Author/s:
Liao, J;Wang, P;Jiang, WJ;Du, X;Liu, JZ;Li, D

Title:
Unraveling the Impact of Electrosorbed Ions on the Scaling Behavior of Fast-Charging Dynamics of Nanoporous Electrodes Toward Digital Design of Iontronic Devices

Date:
2025-09-11

Citation:
Liao, J., Wang, P., Jiang, W. J., Du, X., Liu, J. Z. & Li, D. (2025). Unraveling the Impact of Electrosorbed Ions on the Scaling Behavior of Fast-Charging Dynamics of Nanoporous Electrodes Toward Digital Design of Iontronic Devices. Advanced Materials, 37 (36), https://doi.org/10.1002/adma.202506177.

Persistent Link:
https://hdl.handle.net/11343/362649

ADVANCED MATERIALS
www.advmat.de

Unraveling the Impact of Electrosorbed Ions on the Scaling Behavior of Fast-Charging Dynamics of Nanoporous Electrodes Toward Digital Design of Iontronic Devices

Jinsha Liao, Peiyao Wang, Wen-Jie Jiang, Xiaoyang Du, Jefferson Zhe Liu, and Dan Li**

Electrolyte-filled nanoporous electrodes with fast-charging capability are critical for advanced energy storage and iontronic devices. However, experiments and simulations consistently show that increasing electrode thickness degrades performance by limiting ion access to effective electrode/electrolyte interfaces, especially under fast-charging conditions. While often attributed to sluggish ion transport, the underlying mechanisms and the quantitative link between thickness and performance remain unclear due to complex pore structures and nanoconfined ion dynamics. Here, using multilayered graphene membranes as a model system, modified Poisson–Nernst–Planck simulations with experiments are combined to reveal how electrosorbed ions reshape local electrical and chemical potentials, particularly as the surface-to-volume ratio increases with reduced pore size. It is shown that electrosorbed ions substantially influence the scaling behavior of capacitance across electrode thicknesses, causing marked deviations from classical transmission line models as pores approach nanometric dimensions. Despite the complexity introduced by nanoconfinement, introducing a correction factor enables capacitance–scan rate relationships to collapse into a unified curve across various electrode architectures, allowing computationally efficient design of high-performance fast-charging electrochemical and iontronic devices. This work highlights the unique role of 2D nanomaterials as a versatile platform for bridging experiments and theory to address long-standing challenges in ion transport dynamics.

1. Introduction

Porous electrode materials underpin many electrochemical energy storages and iontronic devices due to their high surface-to-volume ratios, which reinforce the role of fundamental electrode/electrolyte interfaces in determining key properties such as charge storage capacity and interfacial reactions.[1–5] However, the effective utilization of electrode/electrolyte interfaces is ultimately governed by ion transport, particularly under dynamic working conditions. Under time-constrained conditions like fast charging/discharging or in thick electrodes, the finite ion mobility prevents ions from fully traversing the electrode. Experiments consistently show that increasing electrode thickness often leads to severe performance degradation.[6–11] Phenomena such as drastically reduced capacitance in supercapacitors, compromised power density of batteries, and issues like dendrite formation and unstable solid electrolyte interphase due to ion transport limitation and resultant uneven ion distribution in the long term often arise, leading to critical challenges in translating laboratory-scale prototypes into thick electrodes for practical devices.[12–16]

For electrodes with large pore sizes, how their ion transport-dependent performances scale with electrode dimensions can be described by classical theories, such as the Transmission Line Model (TLM) and effective-medium theories.[17,18] These models typically describe ion transport as governed by ohmic resistance or bulk electrolyte diffusion and commonly attribute the degraded performances to terms such as "sluggish ion transport", "ion depletion", or "poor ion accessibility".[10,12,19–26] However, when the

J. Liao, P. Wang, W.-J. Jiang, X. Du, D. Li
Department of Chemical Engineering
The University of Melbourne
Parkville, VIC 3082, Australia
E-mail: dan.li1@unimelb.edu.au, dan.li@ust.hk

The ORCID identification number(s) for the author(s) of this article can be found under https://doi.org/10.1002/adma.202506177

DOI: 10.1002/adma.202506177

D. Li
Department of Chemical and Biological Engineering
The Hong Kong University of Science and Technology
Hong Kong 999077, China

J. Z. Liu
Department of Mechanical Engineering
The University of Melbourne
Parkville, VIC 3082, Australia
E-mail: zhe.liu@unimelb.edu.au

pore sizes reduce to the nanometric scale to further enhance the surface-to-volume ratio or leverage exclusive nanoconfinement effects, electrosorbed ions in the electric double layers (EDLs) can have a significant impact on local electrical and chemical potentials.[27] In such systems, the interface becomes increasingly dominated by these electrosorbed ions, where even EDLs overlap, intensifying surface-related phenomena. The resulting highly nonuniform potentials can fundamentally alter ion transport through the tortuous, interconnected pore networks. These dynamic effects, even without considering additional complex factors like ion correlations or surface interactions, deviating significantly from bulk electrolyte behavior while critical to the performance under dynamic working conditions including fast-charging, cannot be captured by classic models,[28–33] leaving the performance losses insufficiently understood and difficult to predict. Moreover, existing nanoporous materials often exhibit irregular and hierarchical pore structures, making it especially challenging to derive quantitative, physics-based scaling laws.[34]

Recent advances in emerging 2D membranes, exemplified by multilayer graphene, MXene and transition metal dichalcogenides, have enabled the fabrication of nanostructured materials with excellent electrochemical performance and well-defined, interconnected pore networks.[19,35–38] Using these materials, researchers have demonstrated and investigated a variety of unconventional ion transport phenomena, including surface-charge controlled ion transport, ultrahigh ion diffusivity at the atomic scale, and tunable ion sieving via angstrom-scale pore size control.[4,39,40] We have developed freestanding multilayered graphene membranes (MGMs) composed of chemically reduced graphene oxide with tunable sub-10 nm interlayer spacing.[41] Using MGMs as a model system, we have tackled long-standing challenges in ion transport, revealing key mechanisms, including electrostatic gating effects, spatially distinct ionic transport resistance, diffusion-enhanced migrations, and electrosorption-mediated ion transport under fast-charging conditions, advancing both performance optimization through nanostructure tuning and the characterization of charging dynamics.[32,42–44]

In this work, we leverage the well-defined structure and tunable properties of MGM and use MGM-based supercapacitors as a model iontronic system to investigate how electrosorbed ions influence the fast-charging capabilities of nanoporous electrodes, a long-standing challenge that has been difficult to address in the past.[41,45] By combining modified Poisson–Nernst–Planck (mPNP) modeling with experiments,[46,47] we investigate how nanoconfined electrosorbed ions influence the interplay between chemical and electrical potentials, shaping the electrochemical potentials that govern ion transport, and their impacts on the scaling behavior of rate-dependent capacitance under fast charging conditions. We show that electrosorbed ions significantly alter the scaling behavior of capacitance across different electrode thicknesses, leading to pronounced deviations from classical TLM when the pore size falls below 4 nm. Despite the complexity introduced by nanoconfinement, we found that by introducing a correction factor, a unified relationship between capacitance and charging rate across diverse electrode architectures can be established, enabling computationally efficient design of high-performance electrochemical and iontronic devices.

2. Theoretical Analysis of Ion Transport under the Influences of Electrosorbed Ions

Because direct experimental measurement of spatiotemporally resolved ion transport is challenging, we first examine the dynamic capacitance behavior of nanoporous electrodes using a modeling approach based on Poisson–Nernst–Planck (PNP) simulations with steric effects modifications (see details in Methods and Supporting Information).[47] Our system consists of symmetric working and counter electrodes immersed in a 1 M KCl aqueous electrolyte (**Figure 1a**), a model system commonly used to investigate electrochemical behavior under nanoconfinement.[27] The electrode architecture is constructed from interconnected graphene nanoslits, characterized by four key parameters: the size/height of nanoslit d, the lateral size of an intact nanosheet L, aperture size δ, and the number of nanoslits N. We conducted ~600 simulations to vary factors influencing capacitance, including the electrode mass loading/thickness (via the number of nanoslits N), slit size d, intact nanosheet length, reservoir length, intrinsic ion diffusivities, and ion sizes. (Tables S1 and S2, Supporting Information.) Among these simulations, we primarily focused on conditions relevant to fast-charging which are highly sensitive to ion transport and become complex under nanoconfinement, yet are essential to establishing a quantitative, physically-grounded scaling relation for dynamic performances across electrode thicknesses.

We have found that our simulations can successfully capture the key trends of capacitance C under various operational and structural conditions, showing qualitative agreement with experiments. At low scan rates ν, the simulated capacitance remains nearly constant, corresponding to ideal fully charged quasi-equilibrium conditions (Figure 1b). However, beyond a threshold rate $\nu_{\text{tli.}}$, the insufficient charging time hinders ion transport and electrosorption deeper inside the electrode, causing the capacitance to deviate from its ideal value under thermal equilibrium conditions and transition into a rate-dependent regime (Figure 1e). This rate-dependent behavior of capacitance $C(\nu)$ capturing the fundamental transport-limiting behavior critical to fast-charging performance, qualitatively aligns with the MGM experimental capacitance measured via cyclic voltammetry (CV).[41]

Moreover, the complex, nonlinear effects of primary operational and structural factors on capacitance C observed in experiments also emerge in our simulation results (Figure 1e). For instance, the maximum capacitance scales with mass loading N, its rate-dependent variation does not follow a simple trend but instead shows a strong nonlinear dependence on N (Figure S13, Supporting Information). Capacitance decay with increasing ν is more pronounced for thicker electrodes or smaller slit sizes d. For instance, increasing ν from 0.001 to 0.02 V μs^{-1} reduces C by 58.38% for $d = 1.2$ nm and $N = 100$, compared to only 24.52% for $d = 5$ nm. These trends closely match experimental observations, where MGMs with greater mass loadings or smaller interlayer spacings exhibit capacitance decay at smaller charging rates, and this rate is nonlinearly dependent on the N and d.[41]

Beyond macroscopic trends agreeing with experimental results, our simulations reveal microscopic insights into the governing mechanisms of ion transport under confinement, which are unattainable from classic TLM models. Fundamentally, ion

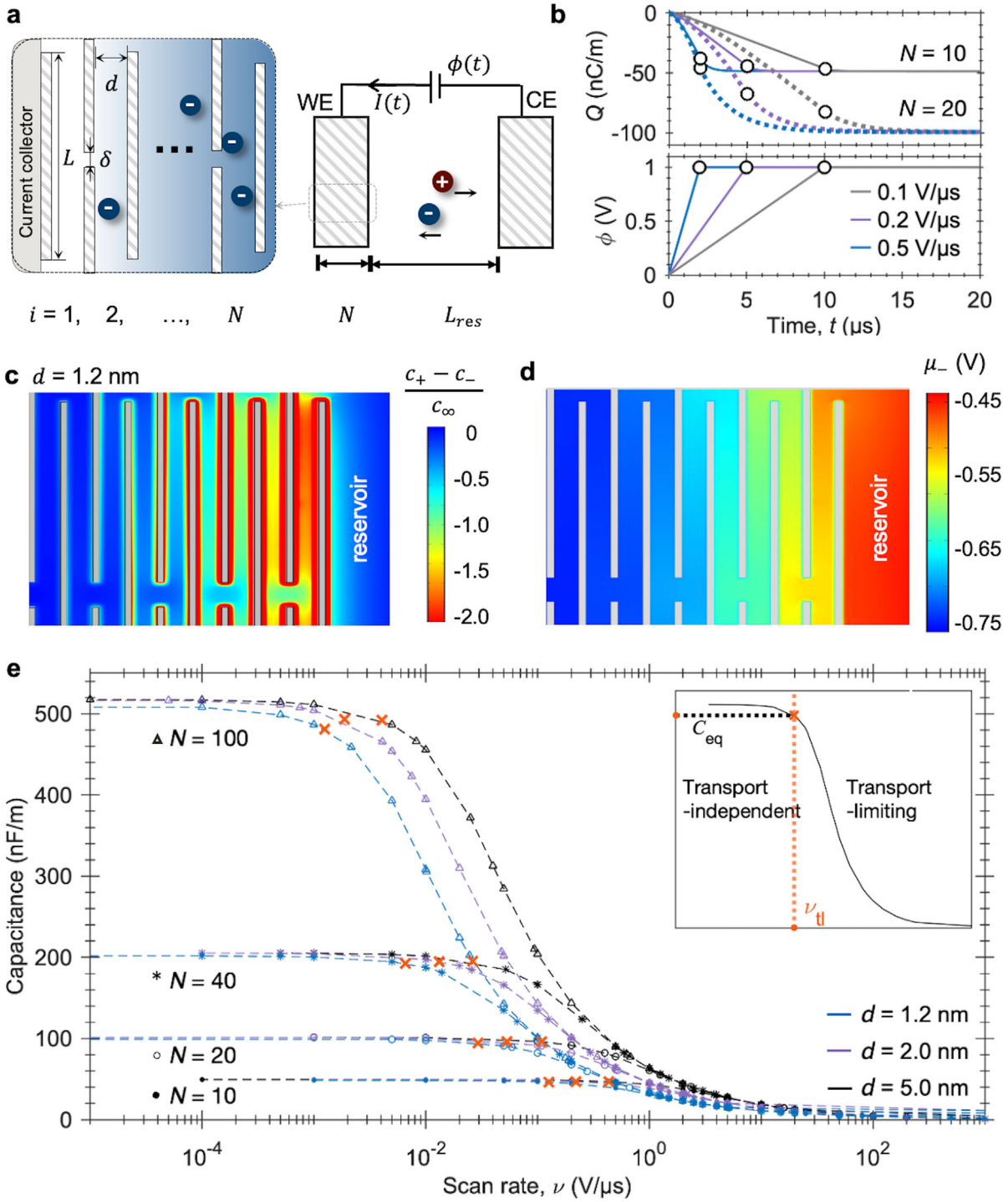

Figure 1. Schematics of the electrified network electrodes and charging profiles. a) Schematics of the cell composed of two symmetric porous electrodes, with a zoomed-in view of the cascading nanoslit network structures. The working electrode (WE) is electrified by an external electric input $\phi(t)$, while the counter electrode (CE) is grounded, leading to an ionic electrical current. Structural parameters are labeled: number of nanoslits N, reservoir length L_{res}, slit size d, aperture size δ, and lateral length of an intact nanosheet L. b) Charge (top) and voltage (bottom) profiles for electrodes with 10 and 20 nanoslits. c) Concentration of electrosorbed ions in EDL, defined as the concentration difference between cations c_+ and anions c_- in electrodes with $d = 1.2$ nm under external applied potential $\phi = 0.8$ V and scan rate $\nu = 0.2$ V μs^{-1}. d) anion electrochemical potential $\mu_- = \frac{RT}{F} \ln \frac{c_-}{c_\infty} - \mu^\phi$ in nanoslit networks shown in (c) at the same instant. All other symbols have their usual definitions. e) Simulated capacitance as a function of scan rate ν for electrodes with varying slit sizes and numbers of nanoslits. Blue, purple, and black curves correspond to slit sizes of $d = 1.2$, 2.0, and 5.0 nm, respectively. Markers represent the number of nanoslits: triangles $N = 100$, asterisks $N = 40$, circles $N = 20$, and dots $N = 10$. Inset: illustration of transport-independent ($C > 0.95C_{eq}$) and transport-limiting ($C \leq 0.95C_{eq}$) regions, with ν_{tl} defined where $C = 0.95C_{\text{eq}}$.

transport is collectively driven by gradients of chemical and electrical potentials, whose interplay defines the electrochemical potentials.[48] In nanoconfined systems, this interplay is significantly modified by electrosorbed ions accumulated within EDLs, in contrast to bulk electrolytes, where uniform ion distributions and electroneutrality preclude such effects.[30,33] By explicitly modeling these electrosorbed ions in nanoslit networks, our framework captures not only their influence on ion transport but also their direct contribution to capacitance, which is determined by the integrated net ionic concentration ($c_+ - c_-$), i.e., the electrosorbed ions themselves. Figure 1c presents a typical example of $d = 1.2$ nm, where the entire transport pathway is dominated by electrosorbed ions during the charging process. At a potential $\phi = 0.8$ V and a high charging rate of 2 V μs^{-1}, our simulation shows that the chemical potential μ_-^{chem} variation is modest, limited 0 to ≈18 mV, while the electric potential in the electrolyte μ^{ϕ} span from ≈−0.74 to −0.52 V. As a result, the electrochemical potential profiles μ_i governing ion transport, which is defined as the sum of μ_i^{chem} and μ^{ϕ}, exhibits spatial variation, ranging from -0.74 V in deeply buried nanoslits to ≈−0.5 V in the nanoslit adjacent to the reservoir (Figure 1d).

These results fundamentally contrast with predictions by the porous electrode theory and TLM.[17,49] In these theories, μ_-^{chem} is 0 due to the assumptions of a uniform bulk electrolyte concentration, and μ^{ϕ} is computed to reach 0.8 V at an applied ϕ = 0.8 V (Figure S8b, Supporting Information). This discrepancy underscores the essential role of electrosorbed ions in modulating μ^{ϕ} and the interplay between chemical and electric potentials, rather than a simple linear superposition. Our previous results further indicate that these electrochemical potentials, mediated by electrosorbed ions, can introduce novel transport mechanisms, significantly influencing macroscale device-level properties.[32,50]

Our results also offer new insights into ion depletion, accessibility, and their roles in governing charging dynamics under fast-charging conditions. It is worth clarifying that the term "ion depletion" can refer to two distinct phenomena: the local depletion of a specific ion species (cations in our case) or the reduction of the total ion population within the pores. In our nanoconfined system, neither of these limits the charging dynamics even under high charging rates. On the one hand, cations undergo noticeable desorption and local depletion near the electrode surface (Figure S10, Supporting Information). Yet, the gradient of the cation electrochemical potential μ_+ indicates this desorption process, essential for effective charge storage, is energetically favored during charging, thereby facilitating charge storage. On the other hand, the total ion population inside the pores does not significantly decrease; in fact, it can even exceed the bulk concentration in smaller slit sizes (Figure S11a,b, Supporting Information), which indicates it not a limiting factor for charge dynamics. In terms of ion accessibility, we observed that in large slit sizes, although a significant number of ions can access the pores, only those near the interfaces contribute effectively to electrosorption. In contrast, with comparable capacitance, most accessible ions in smaller slits are directly involved in electrosorption (Figure S12, Supporting Information). This enhanced utilization of accessible ions also manifests as improved volumetric performance metrics, which will be quantitatively evaluated in the subsequent design analysis.

3. Scaling Analysis for Rate-Dependent Capacitance for Electrodes with Different Thicknesses under the Influences of Electrosorbed Ions

The previous section reveals that the charging dynamics in nanoporous electrodes are governed by complex, spatially varying electrochemical potentials shaped by electrosorbed ions, which do not arise in bulk electrolytes or electrodes with large pores. Building on this, we now focus on their impacts on the scaling behaviors of macroscopic rate-dependent capacitance and mesoscopic charge transport efficiency. We first studied the rate-dependent capacitance $C(\nu)$ for electrodes of varying thicknesses (N = 10 to 100) while keeping the slit size fixed at a relatively large slide size d = 5 nm (**Figure 2a**). In this case, the fraction of electrosorbed ions within the nanoslits is less significant, allowing us to primarily assess the impact of electrode thickness on ion transport and capacitance without strong interference from electrosorption. To characterize how $C(\nu)$ scales with electrode thickness, we focused on whether the ion transport/adsorption timescale τ_{ion} matches the available charging time $\tau_{scan} = \phi_{max}/\nu$. The τ_{ion}, guided by the classic TLM (See details in Experimental section),[17] scales as $(NL)^2/D$, where NL is the primary ion transport/adsorption length in nanoslit networks, and D is the ion diffusivity. This led to a dimensionless scan rate $\nu_d^* = \tau_{ion}/\tau_{scan}$ as in Equation (1),

$$\nu_d^* = \tau_{ion} / \tau_{scan} = \frac{\nu}{\phi_{max}} \frac{(NL)^2}{D} \quad (1)$$

Using this devised scaling relation in Equation (1), we identified the scaling behavior of rate capacitance and mesoscopic charge transport across different thicknesses. Specifically, we found that the relationship between the capacitance C^* and scan rates ν collapses into a single curve across different thicknesses (Figure 2b), confirmed by a high determination of coefficient R^2 > 0.999 (see details in Experimental section). Here C^* is normalized with respect to the material's thermal equilibrium capacitance C_{eq} under fully charging conditions. Moreover, for a given macroscopic C^* value, the mesoscopic charge transport efficiency follows a consistent pattern, regardless of electrode thickness. This is evident from the aligned q^*-x^* curves (Figure 2c), corresponding to circles and crosses on the unified curve in Figure 2b. Notably, this unified pattern remains dynamically consistent throughout the charging process from 0 to 1 V (Figure 2d). The robustness of the devised scaling relation is further confirmed by additional tests varying ion diffusivities $D_{\pm}$, maximum voltage ϕ_{max}, length of the nanoslits L, ion sizes $a_{\pm}$ and reservoir length L_{res} (Figures S3–S7, Supporting Information).

We applied our scaling relation to experimental capacitance measurements and found good agreement with the scaling behavior identified by our simulations. After transformation using the devised scaling relation, experimental C-ν curves for electrodes with the same slit size (~7.7 nm) but different thicknesses (82 and 172 μm; Figure 2e) align well with the simulation produced, unified C^*-ν_d^* relationship (Figure 2f, see details in Methods). This strong agreement (R^2 = 0.9656) suggests that our mPNP-based simulations capture rate-dependent nanoconfined ion transport,

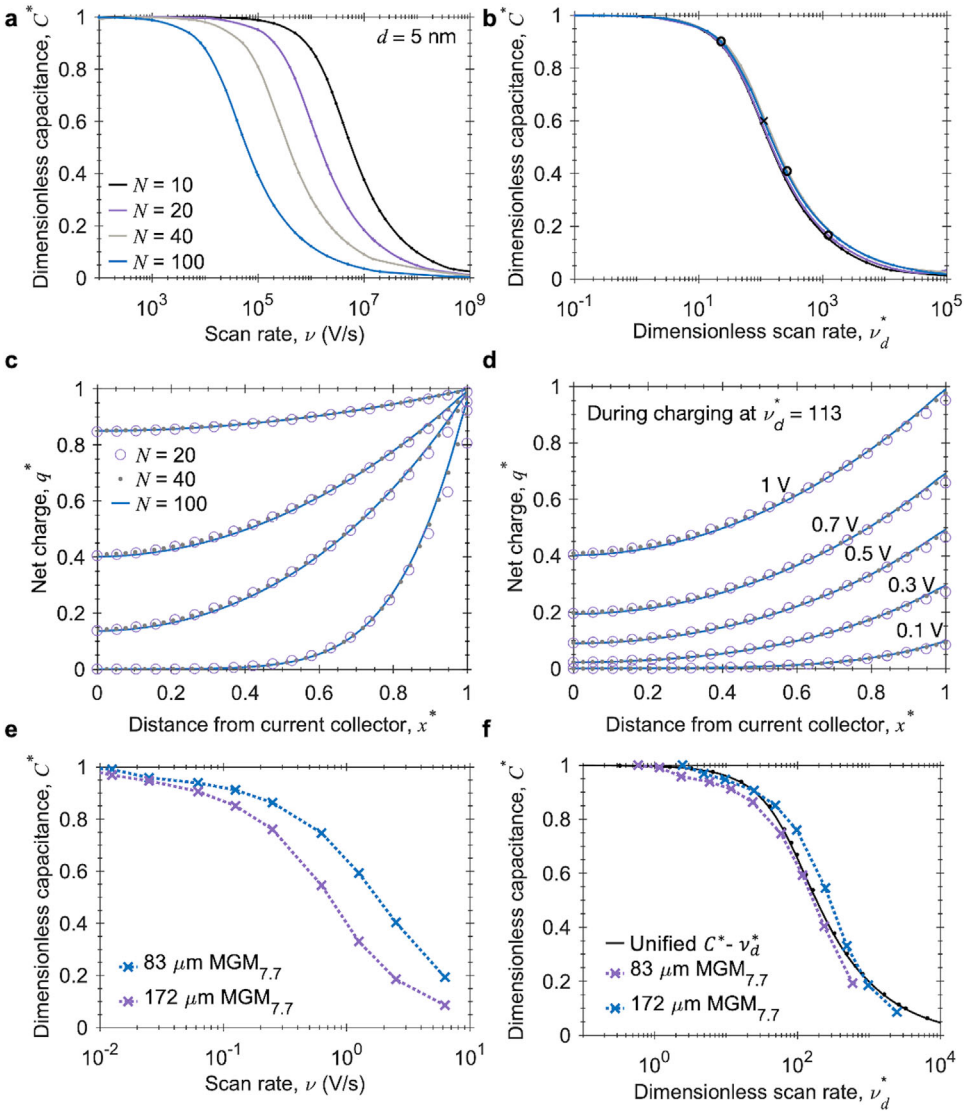

Figure 2. Scaling relation to bridge dynamic performances across varied electrode thicknesses. a) The specific capacitance C^* of electrodes as a function of scan rate ν for electrodes with varying thickness (represented by varying numbers of nanoslits, N = 10, 20, 40, and 100). All electrodes have a fixed slit size d = 5 nm. b) The capacitance of the same electrodes, but now as a function of dimensionless scan rate ν_d^* transformed by scaling relation per Equation (1). c) Mesoscopic charge transport efficiency of electrodes with disparate thicknesses but identical C^*. The net charge distribution q^* along the thickness direction of electrodes with N = 20, 40, and 100 at different values of C^* (15%, 40%, 60%, and 90%), corresponding to the crosses and circles in (b). The y-axis represents the net charge in each nanoslit normalized by the equilibrium-state net charge q_{max}, and the x-axis denotes the relative position of each nanoslit i^{th}/N nanoslit from the current collector. d) Mesoscopic charge distribution during the charging process to 1 V at a scaled scan rate: ν_d^* = 113, corresponding to C^* = 0.6, the cross point labeled in (b). e) The specific capacitance of MGMs with a thickness of 83 and 172 µm in a 1 M KCl aqueous solution plotted against experimental scan rate. f) The rate-dependent capacitance of the same electrodes as in (e), but against dimensionless scan rate transformed using the proposed scaling relation per Equation (1) to compare with the unified C^*-ν_d^* relationship in panel (b). In panels (e) and (f), the specific capacitance is normalized by the maximum capacitance tested at a scan rate ν of 5 mV s^{-1}. These MGMs have close slit sizes of 7.7 nm.

effectively describing the dominant charging dynamics in the experimental thick and bulky nanoporous MGMs.

Next, we examined how slit size could affect scaling behaviors. Previous research works have demonstrated that ion transport under nanoconfinements is complicated and sensitively dependent on slit size due to interfacial electrosorbed ions.[41–43] The reduced cross-section area of nanoslit obviously increases ionic transport resistance. However, the electrosorbed ions lead to increased ion concentration or charge carriers, hence could enhance surface conduction.[27] Our recent studies also reveal the unexpected impact of ion diffusion on ion migration, and this impact is highly dependent on slit size.[32] A time-dependent ionic transport resistance at the nanopore entrance due to EDL overlap has also been reported.[30] These complicated scenarios prompted us to dive into how variations in slit size influence the scaling relation.

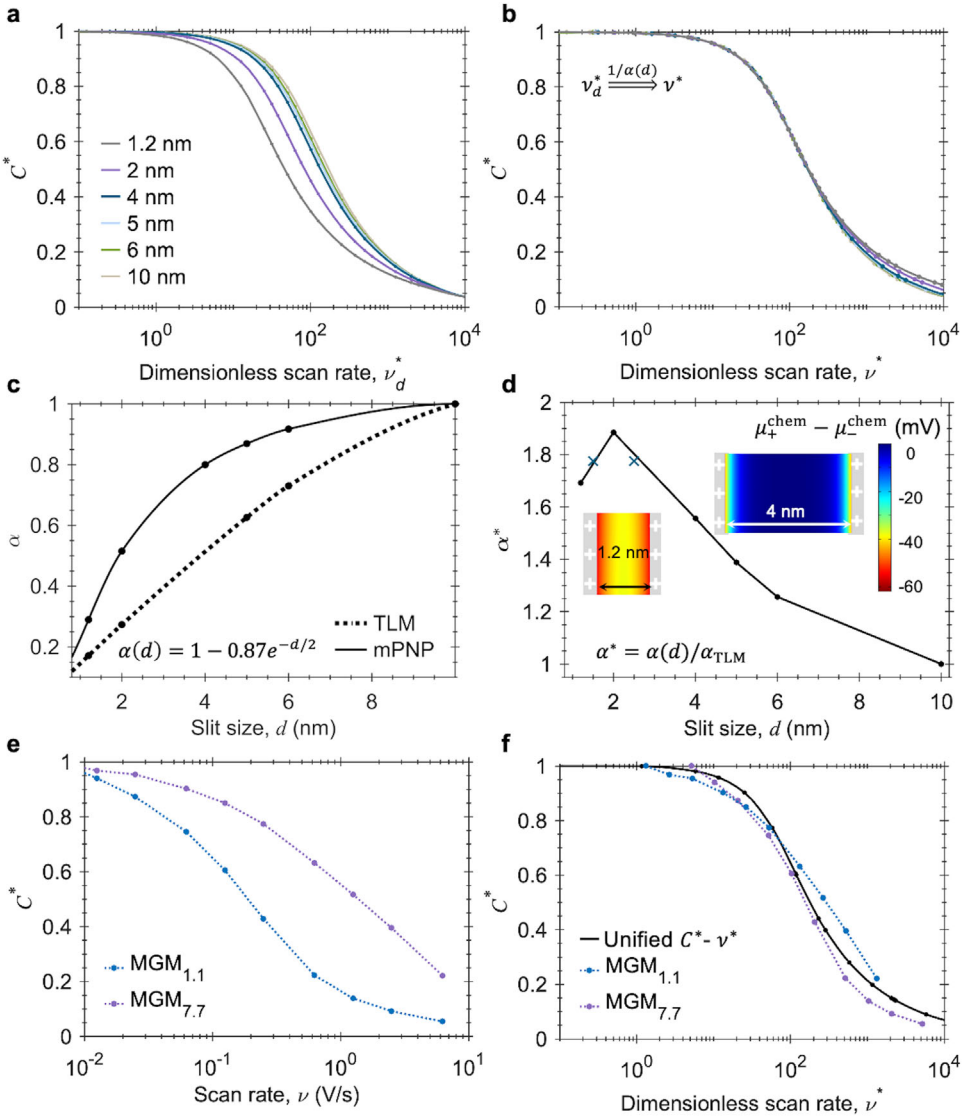

Figure 3. Influences of the slit size on the dynamic performance and the scaling relation for nanoporous electrodes. a) Rate-dependent capacitance of nanoporous electrodes with varying slit sizes (same mass loading $N = 10$). b) Aligned rate-dependent capacitance presented as a function of scan rate ν^* transformed using Equation (1) and coefficient $\alpha(d)$ in (c). c) Slit-size-dependent coefficient $\alpha(d)$ obtained by aligning the rate-dependent capacitance of electrodes with varying slit sizes. The dashed line represents its counterpart predicted by TLM α_{TLM}, which only accounts for the nominal geometric slit size effects on ion transport. d) Enhancement factor $\alpha^* = \alpha(d)/\alpha_{TLM}$ showing the exclusive effects of nanoconfined electrosorbed ions. Cross symbols (at $d = 1.5$ and 2.5 nm) are additional simulations validating the observed maximum near $d = \sim 2$ nm. Inset: the chemical potential differences between counter-ions and co-ions in slits of $d = 1.2$ and 4 nm. e) Experimental rate-dependent capacitance of MGMs with varied interlayer spacing d in an aqueous 1 M KCl solution, with the subscript indicating each MGM's respective d. f) Comparison of the unified C^*-ν^* relationship in panel (b) with the experimental data transformed using the proposed scaling relation and $\alpha(d)$ per Equation (2). The areal mass loading for both MGM$_{1.1}$ and MGM$_{7.7}$ is 0.79 mg cm^{-2}.

We applied the scaling relation in Equation (1) to the electrodes with different slit sizes separately ($d = 1.2$ nm and 2 nm in Figure S14, Supporting Information), successfully unifying the C^*-ν relationship for each case. However, when extending this analysis to a broader slit size range d from 1.2 to 10.0 nm, where continuum theory remains robust,[31,35] we found remarkable deviations for slit sizes below ~4 nm (**Figure 3a**). For slit sizes above ~4 nm, the obtained C^*- ν_d^* relationships exhibit a high degree of overlap with a coefficient of determination of $R^2 = 0.9895$, suggesting that the C^*-ν_d^* relationships can be unified for large slit-size electrodes ($d \geq \sim 4$ nm). The noticeable deviation arises at sub-4 nm levels. For instance, at the same 0.5C^*, ν_d^* for $d = 1.2$ nm is four times smaller than $d = 4$ nm. At $\nu_d^* = 50$, the capacitance C^* for $d = 4$ nm is 34% higher than for $d = 1.2$ nm, but only 7% higher than for $d = 10$ nm.

These deviations indicate that electrosorbed ions under nanoconfinement fundamentally alter the interplay between chemical and electrical potentials, leading to significant departures from classical scaling. While these effects are non-negligible, we found that by introducing a slit size correction

coefficient $\alpha(d)$ into the scaling relation per Equation (2), we could successfully unify C^*-ν_d^* relationships across varying slit sizes. This coefficient α is obtained by collapsing each curve C^*-ν_d^* for electrodes with a different slit size to the one with 10 nm slit size with the largest R^2, which exhibits an exponential relationship with the slit size d (Figure 3c). The well-aligned curves in Figure 3b with $R^2 > 0.999$ affirm the robustness of our approach and the unifiability of the C^*-ν_d^* relationships.

$$\nu^* = \frac{1}{\alpha(d)} \frac{\nu}{\phi_{\max}} \frac{(NL)^2}{(D_+ + D_-)/2} \tag{2}$$

We have attempted to examine this simulation-derived coefficient α by using experimental results of MGMs with two interlayer spacings, as labeled by their subscripts MGM_d. The C-ν curves of $MGM_{1.1}$ and $MGM_{7.7}$ (Figure 3e) are transformed using the slit-size-dependent scaling relation in Equation (2), showing a good agreement ($R^2 = 0.9662$) with the simulation-produced one (Figure 3f). Additionally, we tested this approach using previously reported experimental data,[50] which yielded similarly strong agreement ($R^2 = 0.9577$) with the simulation-derived C^*-ν^* behavior (Figure S8, Supporting Information).

Our scaling relation provides deeper insights into scaling behaviors of charging dynamics under the impacts of electrosorbed ions under nanoconfinement, which were previously unavailable using classic models. This is achieved through explicitly accounting for nanostructures and modelling the electrosorbed ions. Unlike planar or effective media-based porous electrode systems where τ_{ion} linearly scales with the transport length,[28,51,52] we show that τ_{ion} scales with the square of the transport length L in nanoslit networks. Such a quadratic relation means that increasing the transport length of ions in nanoporous electrodes results in both a capacitance decay at lower charging rates and a more pronounced decay magnitude compared to those systems, manifesting as the "sluggish ion transport".[10,12,19–23]

In addition, $\alpha(d)$ provides insights into the contribution of electrosorbed ions into charging dynamics. Compared with the classical TLM prediction $\alpha_{TLM}(d)$ (see details in Supporting Information), which only accounts for the reduced cross-sectional area without considering electrosorbed ions,[17] our results show that $\alpha(d)$ consistently exceeds $\alpha_{TLM}(d)$ when $d < 10$ nm (Figure 3c; Figure S9, Supporting Information). This deviation highlights the additional transport enhancement provided by electrosorbed ions under nanoconfinement.

To further quantify this effect, we define $\alpha^* = \alpha(d)/\alpha_{TLM}(d)$. As shown in Figure 3d, α^* increases to 1.88 at $d = 2$ nm and slightly decreases to 1.68 at $d = 1.2$ nm, clearly demonstrating enhanced charge transport beyond classical expectations. This enhancement correlates with the overlapped EDLs. For $d = 1.2$ nm or 2 nm, overlapped EDLs significantly increase the in-slit net charge concentration and induce noticeable chemical potential differences between counter-ions and co-ions (Figure 3d inset and Figure S15, Supporting Information), unlike the near-zero, uniform profile observed at $d = 4$ nm. Although this enhancement appears linked to surface conduction mechanisms,[29] our data indicate it cannot be solely attributed to increased surface ion concentration. For example, the minimal ion concentration increase in the $d = 4$ nm slit (Figure S14f, Supporting Information) still yields a notable $\alpha^* = 1.55$. Moreover, as d decreases from 2 to 1.2 nm, α^* drops by more than 10% despite a ≈30% rise in total ion concentration (Figure S15d, Supporting Information). These observations suggest that α^* encompasses a range of mechanisms beyond the surface conduction mechanisms, such as the competitive entrance effects[30] and the local charge-dependent dynamic ionic resistance,[32] which warrants further detailed investigations. Yet, as most prior research have focused on ion transport under quasi-equilibrium state or low charging rates, and our recent findings reveal that dominant charging mechanisms are jointly dependent on both slit size and scan rate,[50] the dynamics of electrosorbed ions under non-equilibrium conditions such as fast charging may differ from previously revealed mechanisms. The observed effects of electrosorbed ions $\alpha^*(d)$ in our results likely reflect these complex interactions and warrant further detailed investigation in future studies.

Lastly, two important implications arise. First, while increasing electrode thickness is an intrinsic limitation on charge transport efficiency, nanoconfined electrosorbed ions can partially mitigate this limitation, as reflected by α^*, the factor quantifying the deviation from TLM predictions due to electrosorbed ions. Second, even when the pore size ($d > \sim 4$ nm) is ten times larger than the Debye length (0.3 nm in 1 M electrolyte), these effects remain significant, challenging the common assumption that electrosorbed ions can be neglected in the so-called "thin EDL" regime, where the influences of electrosorbed ions are often neglected.[28]

4. Use of the Scaling Relation for Nanoporous Electrode Design

Improving electrode performance under specific conditions and constraints requires a systematic approach to determine the optimal combination of structural parameters within a high-dimensional parameter space, such as pore size, electrode thickness, charging rate, and packing density. This goes beyond intuitive or simplistic scaling methods. Key performance metrics like energy and power density face well-known trade-offs: thick and dense nanoporous materials, while offering higher energy density, typically suffer from ion transport limitations within a short time that compromises power density.[53,54] In addition, due to the inability to quantitatively predict charge transport efficiency under factors such as mass loading and charging rate, extrapolation of the performance of thick electrodes from thin electrodes observed in lab experiments has been a well-known challenge. The exceptional properties observed in thin samples often diminish when scaled up, resulting in performances comparable to commercial materials.[14]

Moreover, depending on specific application needs, performance metrics vary between gravimetric and volumetric measures. They are often competing and influenced nonlinearly by the packing density (slit size d).[14,41] This means that simplistically scaling up materials can result in inferior performance by both metrics. For instance, thin electrodes with low packing density (large pore size) may achieve exceptional gravimetric capacitance, but these gravimetric values typically do not persist when scaling up, and high porosity also results in low volumetric capacitance.[14]

Quantifying the influences of nanoconfinement effects on ion transport and dynamic performances remains a persistent

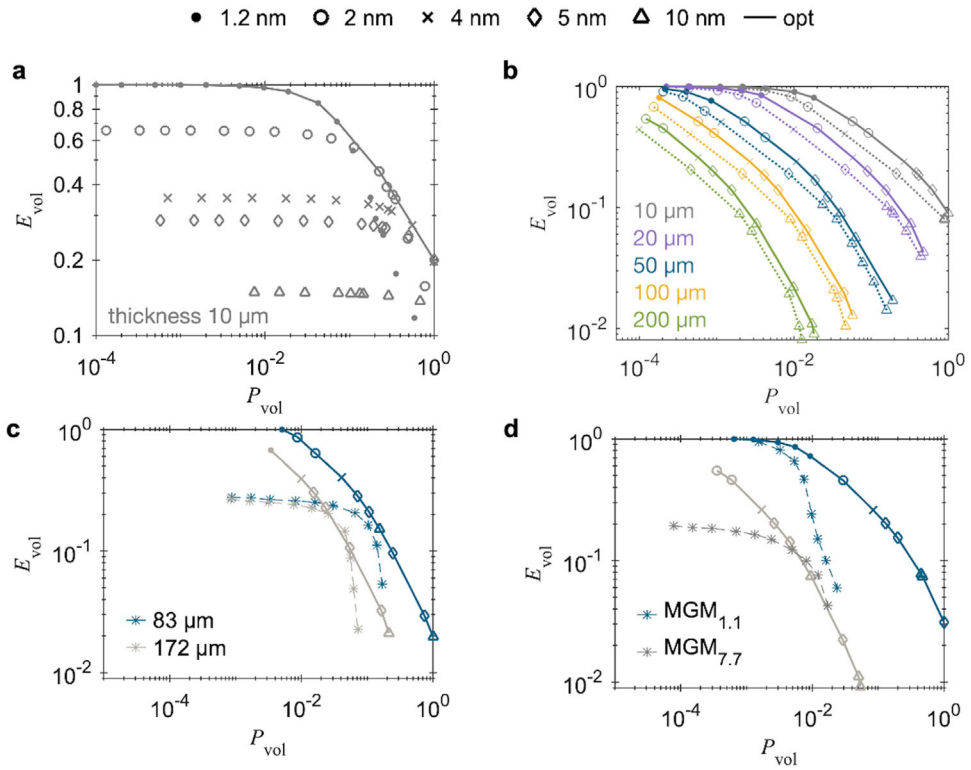

Figure 4. Exploration of Ragone plot and its Pareto frontiers for diverse electrode structures by employing the nanoconfinement-incorporated scaling relation. a) Illustrates volumetric energy and power densities for 10 μm-thick electrodes, with the solid line defining the upper boundary, i.e., Pareto frontier. Diverse slit sizes (d = 1.2, 2.0, 4.0, 5.0, and 6.0 nm) are denoted by distinct markers. Symbols are consistently utilized across all panels. Power and energy densities are normalized to the maximum achievable values. b) Pareto frontiers of varied thicknesses, as denoted by distinctive colors (10, 20, 50, 100, 200 μm). Power and energy densities are normalized to the maximum achievable values for the thinnest electrode. Dashed lines represent TLM predictions. Panels (c) and (d) show simulation-derived frontiers (solid lines) alongside experimental data (dashed lines). The experimental data corresponds to the results of MGMs presented in Figures 2e and 3e.

barrier to developing effective digital strategies for accurate electrode design. Our research provides a numerical strategy. As demonstrated below for some prototypical cases, under given constraints (fixed electrode thickness or mass loading) and target metrics (power and energy densities), we can readily identify the optimal designs (e.g., slit size), including designs with properties that can surpass those of as-synthesized membranes.

As proof of concept, we first demonstrate how the optimal structural parameters vary for target metrics. Consider an electrode with a fixed thickness of 10 μm. There are multiple choices of slit sizes d ranging from 1.2 to 10 nm (**Figure** 4a). For a given slit size d, the electrode achieves a high, nearly constant volumetric energy density E_{vol} at low charging rates, i.e., low power density P_{vol}. Increasing the charging rate increases the P_{vol}, but to certain thresholds E_{vol} begins to drop sharply.

Electrodes with varied d exhibit different power and energy density. Our results show that depending on targeted volumetric energy or power density (E_{vol} or P_{vol}, normalized to the maximum achievable values), optimal slit sizes vary (Figure 4a). Specifically, the constant smallest d cannot always guarantee optimal volumetric energy or power density. For instance, for high $E_{vol} > 0.7$, $d = 1.2$ nm achieves optimal performances, because it simultaneously achieves high P_{vol} compared to other slit sizes (Figure 4a). However, when a higher P_{vol} is demanded ($P_{vol} > 0.2$), $d = 1.2$ nm becomes sub-optimal, providing both lower P_{vol} and E_{vol} compared to 2 and 4 nm.

Here, using our simulated C^*- ν^* relationships, combined with the nanoconfinement-effects-incorporated scaling relation in Equation (2), we crafted Ragone plots that showcase varied electrode structures over a large parameter space, from which the upper boundaries of performances can be derived, namely the Pareto frontier of the Ragone plots as the solid line in Figure 4a.[55] This Pareto frontier indicates the slit size variation for the highest power and energy density under some given constraints and metrics.

Through a series of investigations of different electrode thicknesses, we further demonstrated how our Pareto frontiers can guide the design when varying other constraints. Adjusting electrode thicknesses could be necessary depending on the integrated devices and the interaction with other components, such as separators.[56] Figure 4b shows the P_{vol} and E_{vol} for varied electrode thickness from 10 to 200 μm. The Pareto frontiers clearly indicate the optimal slit size for achieving targeted outcomes, whether aiming for higher or more balanced P_{vol} and E_{vol}.

Notably, the previously identified optimal slit size predicted by the Pareto frontiers in Figure 4a shifts with the different electrode thickness. For instance, as thickness increases from 10 to 200 μm, for P_{vol} no less than 0.2, the optimal slit size shifts from

2 to 5 nm. Interestingly, our exploration range of thickness covers our fabricated MGMs in experiments shown in Figures 2e and 3e. The overlap between the experimental data and the Pareto frontiers in Figure 4c,d validates our prediction of the energy and power densities. Moreover, the Pareto frontiers further indicate that their respective slit sizes are only optimal in these certain regions. Provided that the specifics vary, they become suboptimal. Obtaining these design results would require significant experimental efforts without the predictions provided by our slit-size-dependent relation, which highlights its efficiency in guiding electrode design digitally, especially across diverse conditions and constraints.

Moreover, in addition to identifying the optimal structural parameters, our scaling relation yields valuable physical insights. We explored cases with identical mass loading (number of nanoslits) and evaluated them using gravimetrics (Figure S16, Supporting Information). Changing the evaluation criteria from volumetric to gravimetric uncovers different facets of material utilization. At fixed mass loading, smaller slits almost always outperform larger ones in terms of volumetric performances (Figure S15a, Supporting Information), emphasizing the efficient utilization of electrolyte ions in nanochannels. In contrast, for gravimetric performance considerations, when the electrode thickness is kept constant, larger slit sizes consistently display superior energy and power density (Figure S15b, Supporting Information), highlighting the efficient utilization of electroactive materials.

Furthermore, our experimentally-verified slit-size-dependent scaling relation demonstrates enhanced predictability compared to traditional TLM predictions. Overall, our results forecast Pareto frontiers exceeding those of the traditional TLM predictions in Figure 4b. While TLM generally predicts larger optimal slit sizes, i.e., a more conservative design, our results show that smaller nanoscale slit sizes can achieve outstanding performance. A notable instance is the electrode of 20 µm thickness. Our methods predict its optimal P_{vol} with a slit size $d = 2$ nm to be 100% greater than the TLM prediction $d = 4$ nm at a similar E_{vol}. This, again, underscores the roles of electrosorbed ions as indispensable physical factors under nanoconfinement, even in slit sizes 10 times larger than the Debye length, and the benefits of nanoscale slit sizes in improving dynamic ion transport in porous materials.

In the end, we extended our scaling relation into the sub-nanometer range to examine its applicability and limitations for extreme nanoconfinement scenarios. The slit size effects on dynamic ion transport are informed by simply extrapolating $\alpha(d)$ to the smaller slit sizes. The Ragone plot in Figure S16 (Supporting Information) shows that $MGM_{0.6}$ exhibits superior volumetric performance over $MGM_{1.2}$, regardless of electrode thickness, aligning with the experimental results.[41] Nonetheless, our theoretical estimation of $MGM_{0.6}$'s performance could diverge from experimental results by up to 80%, suggesting that additional nanoscale mechanisms not captured by our mean-field model could become increasingly significant at this scale.

Real MGMs exhibit far greater complexity, including diverse surface functional groups and morphologies, non-uniform pore shapes, hierarchical structure, and slit size distribution extending down to the sub-nanometer level, especially as the interlayer spacing further reduces.[57] The good agreement suggests that our mPNP simulations can capture the dominant slit size effects of the mesoscale cascading nanoslit network on dynamic ion transport for slit sizes above the sub-nanometer level. Novel phenomena beyond our adopted mean-field framework,[58,59] such as the ion-ion correlations,[44] specific adsorption of ions and water molecules,[4,60–62] significant solvent dielectric constant variations,[63,64] and ion dehydration,[65] can exist, may not predominantly influence overall charge transport when the average slit size above sub-nanometer range, or that some of them could offset each other. However, as the confinement intensifies and the slit size approaches the sub-nanometer regime, the significant deviation observed suggests that these mechanisms begin to play a more substantial role. We further note that these atomic and molecular studies have primarily focused on quasi-equilibrium or steady-state properties.[31,44,66–68] In contrast, the role of such effects under non-equilibrium ion transport conditions remains less well understood. We anticipate that bridging these insights with continuum-level modeling will be essential for developing a more complete understanding of transport phenomena in nanoconfined systems.

5. Conclusion

In summary, we employed modified PNP theories and the 2D nanoslit network electrode as a model system of typical ionotronic devices to investigate the effects of electrosorbed ions on the interplay of electric and chemical potential. We systematically explored various structural and operational parameters, revealing their impacts on modifying this interplay and fast-charging dynamics. Capturing this interplay, we developed and applied a scaling relation to unify the rate capacitance for electrodes with varying thicknesses and slit sizes, enabling cross-scale comparisons and offering quantitative insights into nanoconfinement effects on fast-charging dynamics. For slit size d smaller than ~4.0 nm, where in-pore EDL within nanoslit in 1 M KCl overlaps, a new correction factor $\alpha(d)$ is needed to unify the rate capability with different slit sizes. This factor highlights the beneficial effects of electrosorbed ions on charge transport efficiency, mitigating transport restrictions from both reduced cross-sectional area and intrinsic thickness effects. Despite using a simplified model system, the close agreement between the simulated and the experimentally measured rate capacitance of MGMs of different pore sizes and thicknesses demonstrates that nanoslit networks with a small number of nanoslits can reasonably capture the ion transport in the real, thick, porous electrode. Our results further suggest dominant effects of nanoconfined electrosorbed ions on ion transport for $d > 1$ nm can be captured by PNP modeling. For sub-nanometer pores, additional mechanisms enhancing ion transport, likely beyond continuum frameworks, were observed and warrant further investigation. Finally, by utilizing this scaling relation, we demonstrated a numerical optimization strategy for nanoslit network electrode digital designs to search for electrode structures with improved power and energy densities, as demonstrated in Ragone plots. This study also suggests the great potential of the 2D-membrane-based system as a platform to study nanoconfined ion dynamics manifested by its experimental verifiability.

Although our study focused on a purely capacitive model system, driven solely by ion migration, diffusion, and steric effects, the underlying transport mechanisms are fundamental

to a wide spectrum of electrochemical and iontronic devices, such as batteries, electrocatalysts, desalination systems, ionic sensors, and memristors. In these systems, ion transport and the capability of fast-charging influences not just capacitance, but also other key properties like response speed, sensitivity, and dynamic ionic resistance.[12,69–75] While real electrochemical systems involve additional complexities such as redox reactions and multiscale structural heterogeneities, our relatively simple yet representative approach enables the investigation of fundamental transport mechanisms under confinement, obtaining insights that are otherwise difficult to extract in highly disordered systems and laying a foundation for future investigations into such heterogeneities. In particular, the ability to predict rate-dependent ion transport is essential not only for optimizing charge storage, but also for mitigating adverse effects such as polarization, poor power density, and mechanical degradation under rapid operation.[76] Moreover, our findings on α(d) emphasize that the influence of electrode thickness and pore structures is highly sensitive to nanoscale confinement. This insight could facilitate the engineering of cross-scale electrode architectures, such as hierarchical architecture,[77] aligning membranes vertically (pores),[8,78] or drilling holes.[79–81] Scaling relations like ours could serve as a systematic and efficient strategy, particularly as these engineering approaches can be combined for more precisely tailored electrode designs, especially when experimentally screening multiple parameters remains time-consuming and resource-intensive for structurally complex electrodes.

Recent progress in digital design, such as the materials genome approach for 2D materials,[82] has accelerated the discovery of nanoporous electrodes. Yet, predicting and optimizing their dynamic electrochemical performance across structures and operating conditions remains challenging.[83–86] Unlike microelectronics,[87] electrochemical systems lack general scaling laws, as ion transport is highly sensitive to pore geometries and material properties, complicating the design of fast-charging and high-capacity devices. Bridging this gap requires experimentally verifiable and digitizable models that capture the interplay between nanoscale ion dynamics and macroscopic performance. The presented nanoslit network model, combined with our validated scaling relation, offers such a framework, quantitatively connecting simulations and experiments. Integrating this approach with emerging data-driven methods holds promise for advancing the predictive design of next-generation nanoporous electrodes and iontronic devices.[88,89]

6. Experimental Section

Simulations: The continuum simulations are conducted using the mPNP equations per Equation (3) and Equation (4) to study ion transport under the interplay of electric and chemical potentials in the cascading nanoslit network-based electrodes.[32,47,51] Here, D_i, a_i, and z_i represent the diffusion coefficient, ion size, and valency of the i^{th} ion species, respectively. The symbols T, R_u and F denote the temperature, the universal gas constant, and the Faraday constant. Simulations were implemented in the COMSOL Multiphysics package to solve for the spatiotemporal evolution of ion concentration $c_i(x, y, t)$ and electric potential $\phi(x, y, t)$ within the mesoscale heterogeneous nanoslit networks of different thicknesses and slit sizes, with numerous factors varied, such as charging rates. Details of the model systems, simulation parameters, initial and boundary conditions, and numerical methods are provided in the Supporting Information.

$$\nabla \cdot (\epsilon_0 \epsilon_r \nabla \phi) = -eN_A \sum_i z_i c_i \tag{3}$$

$$\frac{\partial c_i}{\partial t} = \nabla \left[D_i \nabla c_i + \frac{z_i D_i F c_i \nabla \phi}{R_u T} + \frac{D_i N_A c_i}{1 - N_A \sum_{i=1}^{2} a_i{}^3 c_i} \sum_{i=1}^{2} a_i{}^3 \nabla c_i \right] \tag{4}$$

In simulations, the working electrode is charged with a potential profile defined as,[90]

$$\phi(t) = \begin{cases} \nu t, & 0 \le t \le \phi_{max}/\nu \\ \phi_{max}, & t > \phi_{max}/\nu \end{cases} \tag{5}$$

where ν is the scan rate and ϕ_{max} is set as 1 V unless otherwise stated. The counter electrode is always grounded.

Calculation of the Ionic Capacitance: In our simulations, the working electrode is charged by a linear sweeping voltage $\phi(t)$ at a scan rate ν to a maximum voltage ϕ_{max} = 1 V unless otherwise stated (Figure 1b). Under electrification ($t > 0$), the charged nanoslit surfaces adsorb/desorb counter-ions/co-ions from/to the reservoir to form EDLs inside the nanoslits. This dynamic process leads to a spatiotemporal evolution of ion distribution enclosed within the nanoslit network, which can be quantitatively described by mPNP theories.

At the end of the sweeping process ($t = \phi_{max}/\nu$), we integrated the net charge accumulated within half electrode, as well as the rate-dependent capacitance accordingly,

$$C = Q/\phi_{max} = \frac{1}{\phi_{max}} \int_{\Omega_{e,w}} F\left(z_+ c_+ + z_- c_-\right) d\Omega \,|t = \frac{\phi_{max}}{\nu} \tag{6}$$

where $\Omega_{e,w}$ is the electrolyte domain in the working electrode region. (See boundary conditions in Figure S1c, Supporting Information).

Scaling Relation Derivation and Effectiveness Evaluation: To obtain this unified C-ν curve, a dimensionless scaling analysis was employed, a well-established practice in physical sciences and engineering, where dimensionless parameters are used to compare competing timescales and processes.[91] The timescale τ_{ion}, guided by TLM, scales as rc.[17] Here, ionic transport resistance r scales with this total transport/adsorption length and inversely with the ion diffusivities D, and the capacitance c also scales with this length, i.e., surface area. For nanoslit networks, τ_{ion} is thus approximately proportional to $rc \approx (NL)^2/D$, where NL is the primary ion transport/adsorption length in nanoslit networks. The comparison between τ_{ion} and τ_{scan} leads to the dimensionless scan rate ν_d^* as in Equation (1).

To evaluate the effectiveness of the scaling relation, we employed the determination R^2.[92] R^2 is calculated by comparing the squared deviations of the C^*-ν_d^* curves for N = 10, 20 and 40 compared against the reference curve N = 100, normalized by the total variance.

Experiments: The MGMs used in this study are freestanding, laminated graphene assemblies prepared via prepared following our previously reported methods.[41] Samples with different interlayer spacings (slit sizes) and mass loadings were fabricated using the same approach. We assembled MGMs via vacuum filtration of chemically converted graphene dispersions. The interlayer spacing and thickness of the MGMs were tuned using a capillary compression technique by adjusting the concentration of H_2O/H_2SO_4 solutions. The average interlayer spacing was estimated based on measured mass loading and thickness using a method described in the Supporting Information (Eq. S8), serving as a statistically averaged descriptor of the interlayer distance across the membrane structure. CV measurements were conducted using a three-electrode system at varying scan rates to determine the rate capacitance of the MGMs in 1 M KCl electrolyte. Detailed procedures for materials synthesis and characterization techniques are provided in the Supporting Information.

Correlating Simulation and Experimental Rate Capacitance: To evaluate how our scaling relation performs with experiments, we compared the simulation-produced unified rate capacitance (C^*-ν_d^*) with the experimental data of MGMs. This is achieved by transforming the experimental charging rates into dimensionless form via employing the scaling relation Equation (2). To employ Equation (2), seven parameters need to be determined. Maximum voltage ϕ_{max} and scan rate ν are parameters determined by experimental CV measurements. The maximum voltage was limited to 0.8 V to avoid water decomposition in the aqueous electrolyte. The experimental scan rates ν are presented in Figure 2e, covering a range that ensures the maximum and decay in capacitance can be captured. The diffusion coefficients $D_{\pm}$ are taken from the 1 M KCl values at room temperature.[93] The slit-size-dependent factor $\alpha(d)$ was derived from simulation results shown in Figure 3c. The number of nanoslits N for real MGMs is determined as,

$$N = \frac{\text{MGM thickness}}{d + h_g} \tag{7}$$

where d and h_g are the interlayer spacing of MGMs and the graphene nanosheet thickness. The lateral length L depends on the fabrication process and remains to be determined. In this work, we treat it as a fitting parameter, aimed at achieving optimal alignment between simulated and experimental C^*-ν_d^* (most significant coefficient of determination R^2). Since L serves as an effective length scale that captures the statistical deviation between idealized nanosheet geometry and real bulk membranes, incorporating the distribution of nanosheet lateral size and shape, molecular corrugation, and intrinsic in-plane pores,[45] L is reasonably treated as a constant, representing the statistically averaged value of each batch of MGMs fabricated. In the fitting, L is determined as 92 nm (MGMs in Figure 2e) and 142 nm (MGMs in Figure 3e), remaining on a comparable scale to the 50 nm identified in our previous investigation.[45]

Supporting Information

Supporting Information is available from the Wiley Online Library or from the author.

Acknowledgements

The authors acknowledge the Australia Research Council (FL180100029, FT220100149, IC180100049, and DP220103498) for financial support.

Open access publishing facilitated by The University of Melbourne, as part of the Wiley - The University of Melbourne agreement via the Council of Australian University Librarians.

Conflict of Interest

The authors declare no conflict of interest.

Data Availability Statement

The data that support the findings of this study are available from the corresponding author upon reasonable request.

Keywords

2D materials, charging dynamics, fast-charging, nanoconfined ion transport, nanoporous materials

Received: April 1, 2025
Revised: May 27, 2025
Published online: June 25, 2025

[1] P. Srimuk, X. Su, J. Yoon, D. Aurbach, V. Presser, *Nat. Rev. Mater.* **2020**, *5*, 517.
[2] J. Wu, H. Liu, W. Chen, B. Ma, H. Ju, *Nat. Rev. Bioeng.* **2023**, *1*, 346.
[3] K. Xiao, C. Wan, L. Jiang, X. Chen, M. Antonietti, *Adv. Mater.* **2020**, *32*, 2000218.
[4] L. Chen, G. Shi, J. Shen, B. Peng, B. Zhang, Y. Wang, F. Bian, J. Wang, D. Li, Z. Qian, G. Xu, G. Liu, J. Zeng, L. Zhang, Y. Yang, G. Zhou, M. Wu, W. Jin, J. Li, H. Fang, *Nature* **2017**, *550*, 380.
[5] P. Simon, Y. Gogotsi, *Nat. Mater.* **2020**, *19*, 1151.
[6] J. Chmiola, C. Largeot, P. L. Taberna, P. Simon, Y. Gogotsi, *Science* **2010**, *328*, 480.
[7] W. Chen, J. Gu, Q. Liu, M. Yang, C. Zhan, X. Zang, T. A. Pham, G. Liu, W. Zhang, D. Zhang, B. Dunn, Y. M. Wang, *Nat. Nanotechnol.* **2022**, *17*, 153.
[8] Y. Xia, T. S. Mathis, M.-Q. Zhao, B. Anasori, A. Dang, Z. Zhou, H. Cho, Y. Gogotsi, S. Yang, *Nature* **2018**, *557*, 409.
[9] H. Li, Y. Tao, X. Zheng, J. Luo, F. Kang, H.-M. Cheng, Q.-H. Yang, *Energy Environ. Sci.* **2016**, *9*, 3135.
[10] Z. Bo, X. Cheng, H. Yang, X. Guo, J. Yan, K. Cen, Z. Han, L. Dai, *Adv. Energy Mater.* **2022**, *12*, 2103394.
[11] Z. Ju, X. Zhang, J. Wu, G. Yu, *Nano Res.* **2021**, *14*, 3562.
[12] Y. Kuang, C. Chen, D. Kirsch, L. Hu, *Adv. Energy Mater.* **2019**, *9*, 1901457.
[13] M. Weiss, R. Ruess, J. Kasnatscheew, Y. Levartovsky, N. R. Levy, P. Minnmann, L. Stolz, T. Waldmann, M. Wohlfahrt-Mehrens, D. Aurbach, M. Winter, Y. Ein-Eli, J. Janek, *Adv. Energy Mater.* **2021**, *11*, 2101126.
[14] Y. Gogotsi, P. Simon, *Science* **2011**, *334*, 917.
[15] M. D. Stoller, R. S. Ruoff, *Energy Environ. Sci.* **2010**, *3*, 1294.
[16] H.-M. Cheng, F. Li, *Science* **2017**, *356*, 582.
[17] R. de Levie, *Electrochim. Acta* **1963**, *8*, 751.
[18] W. Tiedemann, J. Newman, *J. Electrochem. Soc.* **1975**, *122*, 70.
[19] Z. Li, S. Gadipelli, H. Li, C. A. Howard, D. J. L. Brett, P. R. Shearing, Z. Guo, I. P. Parkin, F. Li, *Nat. Energy* **2020**, *5*, 160.
[20] J. Zhu, D. Yang, Z. Yin, Q. Yan, H. Zhang, *Small* **2014**, *10*, 3480.
[21] C. Yan, C. Lv, Y. Zhu, G. Chen, J. Sun, G. Yu, *Adv. Mater.* **2017**, *29*, 1703909.
[22] L. Cong, H. Xie, J. Li, *Adv. Energy Mater.* **2017**, *7*, 1601906.
[23] L. Chang, Y. H. Hu, *Matter* **2019**, *1*, 596.
[24] S. Kim, H. Choi, B. Kim, G. Lim, T. Kim, M. Lee, H. Ra, J. Yeom, M. Kim, E. Kim, J. Hwang, J. S. Lee, W. Shim, *Adv. Mater.* **2023**, *35*, 2206354.
[25] D. B. Robinson, C.-A. M. Wu, B. W. Jacobs, *J. Electrochem. Soc.* **2010**, *157*, A912.
[26] P. Zhu, P. R. Slater, E. Kendrick, *Mater. Des.* **2022**, *223*, 111208.
[27] R. B. Schoch, J. Han, P. Renaud, *Rev. Mod. Phys.* **2008**, *80*, 839.
[28] P. M. Biesheuvel, M. Z. Bazant, *Phys. Rev. E* **2010**, *81*, 031502.
[29] M. Mirzadeh, F. Gibou, T. M. Squires, *Phys. Rev. Lett.* **2014**, *113*, 097701.
[30] A. Gupta, P. J. Zuk, H. A. Stone, *Phys. Rev. Lett.* **2020**, *125*, 076001.
[31] J. Wu, *Chem. Rev.* **2022**, *122*, 10821.
[32] H. Zhan, R. Sandberg, F. Feng, Q. Liang, K. Xie, L. Zu, D. Li, J. Z. Liu, *J. Phys. Chem. C* **2023**, *127*, 13699.
[33] F. Henrique, P. J. Żuk, A. Gupta, *Proc. Natl. Acad. Sci.* **2024**, *121*, 2401656121.
[34] X. Liu, D. Lyu, C. Merlet, M. J. A. Leesmith, X. Hua, Z. Xu, C. P. Grey, A. C. Forse, *Science* **2024**, *384*, 321.
[35] L. Wang, M. S. H. Boutilier, P. R. Kidambi, D. Jang, N. G. Hadjiconstantinou, R. Karnik, *Nat. Nanotechnol.* **2017**, *12*, 509.
[36] H. Zhan, Z. Xiong, C. Cheng, Q. Liang, J. Z. Liu, D. Li, *Adv. Mater.* **2020**, *32*, 1904562.
[37] Y. Kang, Y. Xia, H. Wang, X. Zhang, *Adv. Funct. Mater.* **2019**, *29*, 201902014.
[38] L. Ma, Y. Wang, Y. Liu, *Chem. Rev.* **2024**, *124*, 2583.

[39] M. Zhang, K. Guan, Y. Ji, G. Liu, W. Jin, N. Xu, *Nat. Commun.* **2019**, *10*, 1253.
[40] Y. Xue, Y. Xia, S. Yang, Y. Alsaid, K. Y. Fong, Y. Wang, X. Zhang, *Science* **2021**, *372*, 501.
[41] X. Yang, C. Cheng, Y. Wang, L. Qiu, D. Li, *Science* **2013**, *341*, 534.
[42] J. Xiao, H. Zhan, X. Wang, Z. Q. Xu, Z. Xiong, K. Zhang, G. P. Simon, J. Z. Liu, D. Li, *Nat. Nanotechnol.* **2020**, *15*, 683.
[43] X. Wang, Q. Liang, W. Jiang, P. Wang, J. Liao, Z. Xiong, D. Li, *Small Methods* **2022**, *6*, 2200806.
[44] C. Cheng, G. Jiang, G. P. Simon, J. Z. Liu, D. Li, *Nat. Nanotechnol.* **2018**, *13*, 685.
[45] C. Cheng, G. Jiang, C. J. Garvey, Y. Wang, G. P. Simon, J. Z. Liu, D. Li, *Sci. Adv.* **2016**, *2*, 1501272.
[46] M. S. Kilic, M. Z. Bazant, A. Ajdari, *Phys. Rev. E* **2007**, *75*, 021502.
[47] M. S. Kilic, M. Z. Bazant, A. Ajdari, *Phys. Rev. E* **2007**, *75*, 021503.
[48] A. J. Bard, L. R. Faulkner, *Electrochemical Methods: Fundamentals and Applications*, Wiley, New York, **2001**.
[49] J. S. Newman, C. W. Tobias, *J. Electrochem. Soc.* **1962**, *109*, 1183.
[50] K. Zhang, *Doctor of Philosophy*, Monash University, Melbourne Australia, **2019**.
[51] H. Wang, A. Thiele, L. Pilon, *J. Phys. Chem. C* **2013**, *117*, 18286.
[52] C. Lian, M. Janssen, H. Liu, R. van Roij, *Phys. Rev. Lett.* **2020**, *124*, 076001.
[53] A. Noori, M. F. El-Kady, M. S. Rahmanifar, R. B. Kaner, M. F. Mousavi, *Chem. Soc. Rev.* **2019**, *48*, 1272.
[54] W. Guo, C. Yu, S. Li, J. Qiu, *Energy Environ. Sci.* **2021**, *14*, 576.
[55] M. Ashby, *Materials Selection in Mechanical Design*, Butterworth-Heinemann, Oxford, **2011**.
[56] L. Qu, P. Wang, B. Motevalli, Q. Liang, K. Wang, W.-J. Jiang, J. Z. Liu, D. Li, *Adv. Mater.* **2024**, *36*, 2404232.
[57] Y. Cao, Z. Xiong, F. Xia, G. V. Franks, L. Zu, X. Wang, Y. Hora, S. Mudie, Z. He, L. Qu, Y. Xing, D. Li, *Adv. Funct. Mater.* **2022**, *32*, 2201535.
[58] C. Zhan, C. Lian, Y. Zhang, M. W. Thompson, Y. Xie, J. Wu, P. R. C. Kent, P. T. Cummings, D. Jiang, D. J. Wesolowski, *Adv. Sci.* **2017**, *4*, 1700059.
[59] K. Ge, H. Shao, Z. Lin, P.-L. Taberna, P. Simon, *Nat. Nanotechnol.* **2025**, *20*, 196.
[60] J.-B. Le, Q.-Y. Fan, J.-Q. Li, J. Cheng, *Sci. Adv.* **2020**, *6*, abb1219.
[61] P. Wang, *Atomistic Simulation-Informed Continuum Models for Ion Distribution in Water-Filled Graphene Nanoslits and at Graphene Surfaces*, University of Melbourne, Melbourne Australia, **2020**.
[62] P. Wang, G. Jiang, Y. Yan, L. Qu, X. Du, D. Li, J. Z. Liu, arXiv:2411.13747 **2024**.
[63] G. Gonella, E. H. G. Backus, Y. Nagata, D. J. Bonthuis, P. Loche, A. Schlaich, R. R. Netz, A. Kühnle, I. T. McCrum, M. T. M. Koper, M. Wolf, B. Winter, G. Meijer, R. K. Campen, M. Bonn, *Nat. Rev. Chem.* **2021**, *5*, 466.
[64] L. Fumagalli, A. Esfandiar, R. Fabregas, S. Hu, P. Ares, A. Janardanan, Q. Yang, B. Radha, T. Taniguchi, K. Watanabe, G. Gomila, K. S. Novoselov, A. K. Geim, *Science* **2018**, *360*, 1339.
[65] J. Chmiola, C. Largeot, P.-L. Taberna, P. Simon, Y. Gogotsi, *Angew. Chem., Int. Ed.* **2008**, *47*, 3392.
[66] J. Chmiola, G. Yushin, Y. Gogotsi, C. Portet, P. Simon, P. L. Taberna, *Science* **2006**, *313*, 1760.
[67] S. Faucher, N. Aluru, M. Z. Bazant, D. Blankschtein, A. H. Brozena, J. Cumings, J. Pedro de Souza, M. Elimelech, R. Epsztein, J. T. Fourkas, A. G. Rajan, H. J. Kulik, A. Levy, A. Majumdar, C. Martin, M. McEldrew, R. P. Misra, A. Noy, T. A. Pham, M. Reed, E. Schwegler, Z. Siwy, Y. Wang, M. Strano, *J. Phys. Chem. C* **2019**, *123*, 21309.
[68] P. Robin, L. Bocquet, *J. Chem. Phys.* **2023**, *158*, 160901.
[69] Y. Liu, Y. Zhu, Y. Cui, *Nat. Energy* **2019**, *4*, 540.
[70] R. Tian, S.-H. Park, P. J. King, G. Cunningham, J. Coelho, V. Nicolosi, J. N. Coleman, *Nat. Commun.* **2019**, *10*, 1933.
[71] J. Wu, X. Zhang, Z. Ju, L. Wang, Z. Hui, K. Mayilvahanan, K. J. Takeuchi, A. C. Marschilok, A. C. West, E. S. Takeuchi, G. Yu, *Adv. Mater.* **2021**, *33*, 2101275.
[72] H. Chen, X. Liang, Y. Liu, X. Ai, T. Asefa, X. Zou, *Adv. Mater.* **2020**, *32*, 2002435.
[73] N. Wongkaew, M. Simsek, C. Griesche, A. J. Baeumner, *Chem. Rev.* **2019**, *119*, 120.
[74] T. Mei, W. Liu, G. Xu, Y. Chen, M. Wu, L. Wang, K. Xiao, *ACS Nano* **2024**, *18*, 4624.
[75] P. Li, Y. Jiao, J. Huang, S. Chen, *JACS Au* **2023**, *3*, 2640.
[76] K. P. C. Yao, J. S. Okasinski, K. Kalaga, I. A. Shkrob, D. P. Abraham, *Energy Environ. Sci.* **2019**, *12*, 656.
[77] H. Sun, J. Zhu, D. Baumann, L. Peng, Y. Xu, I. Shakir, Y. Huang, X. Duan, *Nat. Rev. Mater.* **2018**, *4*, 45.
[78] Y. Zhu, Z. Ju, X. Zhang, D. M. Lutz, L. M. Housel, Y. Zhou, K. J. Takeuchi, E. S. Takeuchi, A. C. Marschilok, G. Yu, *Adv. Mater.* **2020**, *32*, 1907941.
[79] L. Peng, Z. Fang, Y. Zhu, C. Yan, G. Yu, *Adv. Energy Mater.* **2018**, *8*, 1702179.
[80] H. Sun, L. Mei, J. Liang, Z. Zhao, C. Lee, H. Fei, M. Ding, J. Lau, M. Li, C. Wang, X. Xu, G. Hao, B. Papandrea, I. Shakir, B. Dunn, Y. Huang, X. Duan, *Science* **2017**, *356*, 599.
[81] Y. Xu, Z. Lin, X. Zhong, X. Huang, N. O. Weiss, Y. Huang, X. Duan, *Nat. Commun.* **2014**, *5*, 4554.
[82] K. M. Jablonka, D. Ongari, S. M. Moosavi, B. Smit, *Chem. Rev.* **2020**, *120*, 8066.
[83] A. A. Franco, A. Rucci, D. Brandell, C. Frayret, M. Gaberscek, P. Jankowski, P. Johansson, *Chem. Rev.* **2019**, *119*, 4569.
[84] Y. Liu, B. Guo, X. Zou, Y. Li, S. Shi, *Energy Storage Mater.* **2020**, *31*, 434.
[85] E. O. Pyzer-Knapp, J. W. Pitera, P. W. J. Staar, S. Takeda, T. Laino, D. P. Sanders, J. Sexton, J. R. Smith, A. Curioni, *Npj Comput. Mater.* **2022**, *8*, 84.
[86] J. Wang, V. Malgras, Y. Sugahara, Y. Yamauchi, *Nat. Commun.* **2021**, *12*, 3563.
[87] R. H. Dennard, F. H. Gaensslen, H.-N. Yu, V. L. Rideout, E. Bassous, A. R. LeBlanc, *IEEE J. Solid-State Circuits* **1974**, *9*, 256.
[88] X. Xie, A. Samaei, J. Guo, W. K. Liu, Z. Gan, *Nat. Commun.* **2022**, *13*, 7562.
[89] Y. Li, Z. Li, R. P. Misra, C. Liang, A. J. Gillen, S. Zhao, J. Abdullah, T. Laurence, J. A. Fagan, N. Aluru, D. Blankschtein, A. Noy, *Nat. Mater.* **2024**, *23*, 1123.
[90] K. Breitsprecher, C. Holm, S. Kondrat, *ACS Nano* **2018**, *12*, 9733.
[91] G. I. Barenblatt, *Scaling, Self-Similarity, and Intermediate Asymptotics*, Cambridge University Press, Cambridge, UK, **1996**.
[92] N. R. Draper, H. Smith, in *Applied Regression Analysis*, John Wiley & Sons, Ltd, Chichester, United Kingdom **1998**.
[93] J. Rumble, *CRC Handbook of Chemistry and Physics*, CRC Press, Boca Raton, FL, **2023**.